The Astrophysical Journal, 687:608–622, 2008 November 1
© 2008. The American Astronomical Society. All rights reserved. Printed in U.S.A.

COLLISIONAL AND THERMAL EMISSION MODELS OF DEBRIS DISKS: TOWARD PLANETESIMAL POPULATION PROPERTIES

Alexander V. Krivov, Sebastian Müller, Torsten Löhne, and Harald Mutschke
Astrophysikalisches Institut und Universitätssternwarte, Friedrich Schiller University Jena,
Schillergäßchen 2–3, 07745 Jena, Germany; krivov@astro.uni-jena.de
Received 2008 May 21; accepted 2008 July 2

ABSTRACT

Debris disks around main-sequence stars are believed to derive from planetesimal populations that have accreted at early epochs and survived possible planet formation processes. While debris disks must contain solids in a broad range of sizes—from big planetesimals down to tiny dust grains—debris disk observations are only sensitive to the dust end of the size distribution. Collisional models of debris disks are needed to "climb up" the ladder of the collisional cascade, from dust toward parent bodies, representing the main mass reservoir of the disks. We have used our collisional code to generate five disks around a Sun-like star, assuming planetesimal belts at 3, 10, 30, 100, and 200 AU with 10 times the Edgeworth-Kuiper Belt mass density, and to evolve them for 10 Gyr. Along with an appropriate scaling rule, this effectively yields a three-parametric set of reference disks (initial mass, location of planetesimal belt, and age). For all the disks, we have generated spectral energy distributions (SEDs), assuming homogeneous spherical astrosilicate dust grains. A comparison between generated and actually observed SEDs yields estimates of planetesimal properties (location, total mass, etc.). As a test and a first application of this approach, we have selected five disks around Sun-like stars with well-known SEDs. In four cases, we have reproduced the data with a linear combination of two disks from the grid (an "asteroid belt" at 3 AU and an outer "Kuiper Belt"); in one case a single, outer component was sufficient. The outer components are compatible with "large Kuiper Belts" of 0.2–50 Earth masses (in bodies up to 100 km in size) with radii of 100–200 AU.

Subject headings: circumstellar matter — planetary systems: formation — Kuiper Belt — stars: individual (HD 377, HD 70573, HD 72905, HD 107146, HD 141943)

1. INTRODUCTION

Since the *IRAS* discovery of the excess infrared emission around Vega by Aumann et al. (1984), infrared surveys with *IRAS*, *ISO*, *Spitzer*, and other space-based and ground-based telescopes have shown the Vega phenomenon to be common for main-sequence stars (e.g., Meyer et al. 2004; Beichman et al. 2005; Najita & Williams 2005; Rieke et al. 2005; Bryden et al. 2006; Siegler et al. 2007; Su et al. 2006; Trilling et al. 2007, 2008; Hillenbrand et al. 2008). The observed excesses are attributed to circumstellar disks of second-generation dust, sustained by numerous planetesimals in orbit around the stars. Jostling collisions between planetesimals grind them all the way down to smallest dust grains which are then blown away by stellar radiation. While the bulk of such a debris disk's mass is hidden in invisible parent bodies, the observed luminosity is dominated by small particles at dust sizes. Hence, the studies of dust emission have the potential to shed light onto the properties of parent planetesimal populations, as well as planets that may shape them, and, ultimately, onto the evolutionary history of circumstellar planetary systems.

However, there is no direct way to infer the properties of invisible planetesimal populations from the observed dust emission. Dust and planetesimals can only be linked through models. First, dynamical models can be used to predict, for a given planetesimal family (mass, location, age, etc.), the distribution of dust. Such models have become available in recent years (e.g., Thébault et al. 2003; Krivov et al. 2006; Thébault & Augereau 2007; Wyatt et al. 2007; Löhne et al. 2008). After that, standard thermal emission models will describe the resulting dust emission. Comparison of that emission to the one actually observed would then reveal the probable properties of underlying, dust-producing planetesimal families.

In this paper we follow this approach and generate a set of hypothetical debris disks around G2 dwarfs with different ages (10 Myr–10 Gyr), assuming debris dust to stem from planetesimal belts with different initial masses at different distances from the central star. For every set of these parameters, we simulate steady-state dust distributions with our collisional code (Krivov et al. 2005, 2006; Löhne et al. 2008). This is different from a traditional, "empirical" approach, in which dust distributions are postulated, usually in form of power laws, parameterized by ranges and exponents that play the role of fitting parameters (e.g., Wolf & Hillenbrand 2003). Interestingly, replacing formal dust distributions with those coming out of dynamical modeling does not increase the number of fitting parameters. Just the opposite: the number of parameters reduces and those parameters that we keep free all have clear astrophysical meaning. The most important are the location of the parent planetesimal belt and its current mass (Wyatt et al. 2007).

Having produced a set of model debris disks, we compute thermal emission fluxes in a wide range of wavelengths from mid-infrared to millimeter. In so doing, we completely abandon simple blackbody or modified blackbody calculations and solve a thermal balance equation instead. At this stage, we assume compact spherical grains composed of astronomical silicate (Laor & Draine 1993) and employ standard Mie calculations to compute dust opacities. Although this is still a noticeable simplification, it represents a natural step toward considering realistic materials and using more involved methods of light-scattering theory that we leave for subsequent papers.

As a test and a first application of the results, we reinterprete available observational data on a selection of disks around Sun-like stars with well-known spectral energy distributions (SEDs).

This paper is organized as follows. Section 2 describes the dynamical and thermal emission models. In § 3 a set of reference

disks is introduced and the model parameters are specified. Section 4 presents the modeling results for this set of disks: size and spatial distribution of dust, dust temperatures, and the generated SEDs. Application to selected observed disks is made in § 5. Section 6 summarizes the paper.

2. MODEL

2.1. *Dynamical Model*

To simulate the dust production by the planetesimal belt and the dynamical evolution of a disk, we use our collisional code (ACE [Analysis of Collisional Evolution]). The code numerically solves the Boltzmann-Smoluchowski kinetic equation to evolve a disk of solids in a broad range of sizes (from smallest dust grains to planetesimals), orbiting a primary in nearly Keplerian orbits (gravity + direct radiation pressure + drag forces) and experiencing disruptive and erosive (cratering) collisions. Collision outcomes are simulated with available material- and size-dependent scaling laws for fragmentation and dispersal in both strength and gravity regime. The current version implements a three-dimensional kinetic model, with masses, semimajor axes, and eccentricities as phase-space variables. This approach automatically enables a study of the simultaneous evolution of mass, spatial, and velocity distribution of particles. The code is fast enough to easily follow the evolution of a debris disk over gigayear timescales. A detailed description of our approach, its numerical implementation, and astrophysical applications can be found in our previous papers (Krivov et al. 2000, 2005, 2006; Löhne et al. 2008).

2.2. *Thermal Emission Model*

For spherical dust grains with radius s and temperature T_g we can calculate their distance r to the star under the assumption of thermal equilibrium as

$$r = \frac{R_*}{2}\sqrt{\frac{\int_0^\infty d\lambda Q_\lambda^{\rm abs}(s) F_{\lambda,*}(T_*)}{\int_0^\infty d\lambda Q_\lambda^{\rm abs}(s) B_\lambda(T_g)}}. \quad (1)$$

Here R_* denotes the radius, $F_{\lambda,*}(T_*)$ the flux of the star with an effective temperature T_*, and $B_\lambda(T_g)$ the Planck function. The absorption efficiency $Q_\lambda^{\rm abs}(s)$ is a function of wavelength λ and particle size.

We now consider a rotationally symmetric dust disk at a distance D from the observer. Denote by $N(r, s)$ the surface number density of grains with radius s at a distance r from the star, so that $N(r, s)ds$ is the number of grains with radii $[s, s + ds]$ in a narrow annulus of radius r, divided by the surface area of that annulus. Then the specific flux emitted from the entire disk at a given wavelength can be calculated as

$$F_{\lambda,\rm disk}^{\rm tot} = \int dr \int ds\, F_{\lambda,\rm disk}(r, s) \quad (2)$$

$$= \frac{2\pi^2}{D^2}\int dT_g\, r(T_g)\frac{dr(T_g)}{dT_g}\int ds\, s^2 \times N(r, s) Q_\lambda^{\rm abs}(s) B_\lambda(T_g). \quad (3)$$

3. REFERENCE DISKS

3.1. *Central Star*

The parameters of the central star (mass and photospheric spectrum) affect both the dynamics of solids (by setting the scale of orbital velocities and determining the radiation pressure strength) and their thermal emission (by setting the dust grain temperatures). We take the Sun (a G2 V dwarf with a solar metallicity) as a central star and calculate its photospheric spectrum with the NextGen grid of models (Hauschildt et al. 1999).

3.2. *Forces*

In the dynamical model, we include central star's gravity and direct radiation pressure. We switch off the drag forces (both the Poynting-Robertson and stellar wind drag), which are of little importance for the optical depths in the range from $\sim 10^{-5}$ to $\sim 10^{-3}$) considered here (Artymowicz 1997; Krivov et al. 2000; Wyatt 2005).

3.3. *Collisions*

The radii of solids in every modeled disk cover the interval from 0.1 μm to 100 km. The upper limit of 100 km is justified by the fact that planetesimal accretion models predict larger objects to have a steeper size distribution and thus to contribute less to the mass budget of a debris disk (e.g., Kenyon & Luu 1999b). To describe the collisional outcomes, we make the same assumptions as in Löhne et al. (2008). This applies, in particular, to the critical energy for disruption and dispersal, $Q_D^*(s)$, as well as to the size distribution of fragments of an individual collision. However, in contrast to Löhne et al. (2008), where only catastrophic collisions were taken into account, we include here cratering collisions as well. This is necessary, as cratering collisions alter the size distribution of dust in the disk markedly, which shows up in the SEDs (Thébault et al. 2003; Thébault & Augereau 2007). The actual model of cratering collisions used here is close to that by Thébault & Augereau (2007). An essential difference is our assumption of a single power law for the size distribution of the fragments of an individual collision instead of the broken power law proposed originally in Thébault et al. (2003). However, this difference has little effect on the resulting size distribution in collisional equilibrium.

3.4. *Optical Properties of Dust*

An important issue is a choice of grain composition and morphology. These affect both the dynamical model (through radiation pressure efficiency as well as bulk density) and thermal emission model (through absorption efficiency). Here we assume compact spherical grains composed of astronomical silicate (aka astrosilicate or astrosil; Laor & Draine 1993), similar to the $MgFeSiO_4$ olivine, with a density of 3.3 g cm^{-3}. Taking optical constants from Laor & Draine (1993) we calculated radiation pressure efficiency $Q_{\rm pr}$ and absorption efficiency $Q_{\rm abs}$ with a standard Mie routine (Bohren & Huffman 1983).

To characterize the radiation pressure strength, it is customary to use the radiation pressure to gravity ratio β (Burns et al. 1979), which is independent of distance from the star and, for a given star, only depends on $Q_{\rm pr}$ and particle size. If grains that are small enough to respond to radiation pressure derive from collisions of larger objects in nearly circular orbits, they will get in orbits with eccentricities $e \sim \beta/(1 - \beta)$. This implies that grains with $\beta < 0.5$ remain orbiting the star, whereas those with $\beta > 0.5$ leave the system in hyperbolic orbits. The β ratio for compact astrosil grains, computed from $Q_{\rm pr}$, is shown in Figure 1. The blowout limit, $\beta = 0.5$, corresponds to the grain radius of $s = 0.4$ μm. Note that the tiniest astrosil grains ($\lesssim 0.1$ μm) would have $\beta < 0.5$ again and thus could orbit the star in bound orbits. However, the dynamics of these small motes would be subject to a variety of effects (e.g., the Lorentz force) not included in our model, and their lifetimes may be shortened by erosion processes (e.g., stellar wind sputtering). Altogether, we expect them to make little contribution

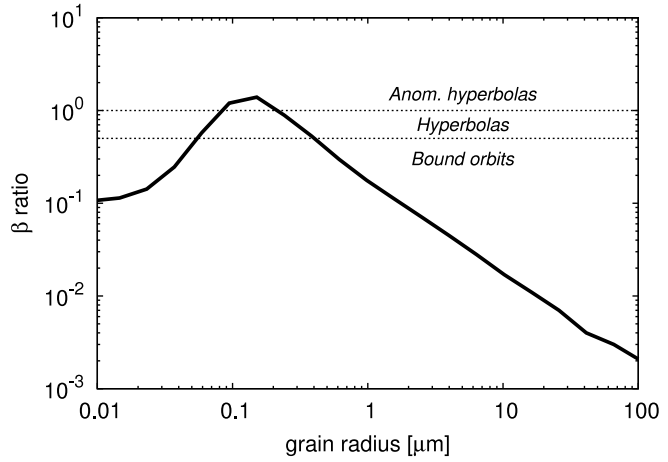

FIG. 1.—Radiation pressure to gravity ratio β for astrosilicate grains as a function of their size. Horizontal lines at $\beta = 0.5$ and 1.0 show which particles typically move in bound elliptic orbits, in hyperbolas, as well as in anomalous hyperbolas (open outward from the star).

to the thermal emission in the mid-IR to submillimeter. By setting the minimum radius of grains to 0.1 μm, we therefore do not take into account these grains here.

The spectral dependence of the absorption efficiency $Q_{\rm abs}$ of different-sized astrosil spheres is depicted in Figure 2.

3.5. *Parent Planetesimal Belts*

To have a representative set of "reference" debris disks around Sun-like stars, we consider possible planetesimal rings centered at the semimajor axes of $a = 3$, 10, 30, 100, and 200 AU from the primary. All five rings are assumed to have the same relative width initially (again, in terms of semimajor axis) of $\Delta a/a = 0.2$ (± 0.1) and share the same semiopening angle (the same as the maximum orbital inclination of the objects) of $\varepsilon = 0.1$ rad. The orbital eccentricities of planetesimals are then distributed uniformly between 0.0 and 0.2, in accordance with the standard equipartition condition. The initial (differential) mass distribution of all solids is given by a power law with the index 1.87, a value that accounts for the modification of the classical Dohnanyi's (1969) 1.833 through the size dependence of material strength (see, e.g., Durda & Dermott 1997).

The initial disk mass is taken to be 1 $M_\oplus$ (Earth mass) for a 30 AU ring, roughly corresponding to 10 (or slightly more) times the Edgeworth-Kuiper Belt (EKB) mass (e.g., Gladman et al. 2001; Hahn & Malhotra 2005). For other parent ring locations, the initial mass is taken in such a way as to provide approximately the same spatial *density* of material. Since the circumference of a ring $2\pi a$, its absolute width Δa, and its vertical thickness $2a\varepsilon$ are all proportional to a, the condition of a constant density requires the mass scaling $\propto a^3$. This corresponds to the initial mass ranging from $\approx 0.001\ M_\oplus$ in the 3 AU case to $\approx 200\ M_\oplus$ in the 200 AU case. With these values, all reference disks have about 10 times the EKB density (10 EKBD).

That all the belts share the same volume density of material is purely a matter of convention. Instead, we could choose them to have the same surface density or the same total mass. Given the scaling rules, as discussed in the text and Appendix A, none of these choices would have strong advantages or disadvantages.

All five reference disks are listed in Table 1. We evolved them with the collisional code, ACE, and stored all results between the ages of 10 Myr and 10 Gyr at reasonable time steps. In what follows, we use self-explanatory identifiers like 10EKBD at 10 AU at 300 Myr to refer to a particular disk of a particular age.

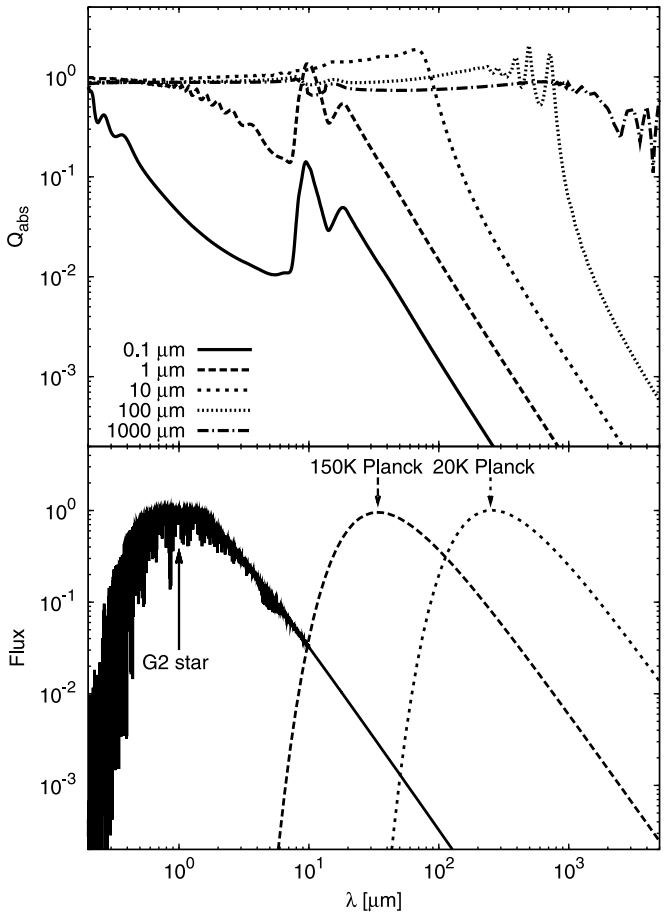

FIG. 2.—*Top*: Absorption efficiency of astrosilicate compact spherical grains as a function of wavelength for different grain sizes. *Bottom*: Spectrum of a G2 V star and the Planck curves for 150 and 20 K (in arbitrary vertical scale) to indicate the spectral ranges most important for absorption and emission.

Importantly, the same runs of the collisional code automatically provide the results for disks of any other initial density (or mass). This is possible due to the mass-time scaling of Löhne et al. (2008), which can be formulated as follows. Denote by $M(M_0, t)$ the mass that a disk with initial mass M_0 has at time t. Then, the mass of another disk with x times larger initial mass at time instant t/x is simply

$$M(xM_0, t/x) = xM(M_0, t). \tag{4}$$

For instance, the mass of the 1EKBD at 10 AU at 10 Gyr disk is one-tenth of the 10EKBD at 10 AU at 1 Gyr disk mass. Note that the same scaling applies to any other quantity directly proportional to the amount of disk material. In other words, M may equally stand for the mass of dust, its total cross section, thermal radiation flux, etc. See Appendix A for additional explanations.

4. RESULTS

4.1. *Size and Spatial Distributions of Dust*

As noted above, the collisional code ACE uses masses and orbital elements of disk particles as phase-space variables. At any time instant, their phase-space distribution is transformed to usual mass/size and spatial distributions. It is important to understand that mass/size distributions and spatial distributions cannot, generally, be decoupled from each other. Grains of different sizes have different radial distributions and, conversely, the size distribution of material is different at different distances from the star.

TABLE 1
Description of Reference Disks

Disk Identifier	Belt Location (AU)	Initial Disk Mass ($M_\oplus$)	a Range (AU)	r Range (AU)
10EKBD at 3 AU	3	0.001	0.3–30	0.5–20
10EKBD at 10 AU	10	0.03	1–100	2–50
10EKBD at 30 AU	30	1	3–300	5–200
10EKBD at 100 AU	100	30	10–1000	20–500
10EKBD at 200 AU	200	200	20–2000	30–1000

A typical size distribution of solids is shown in Figure 3 for one of the disks, namely, 10EKBD at 30 AU at 100 Myr. Different lines correspond to different distances from the primary. As expected, the size distribution is the broadest within the parent ring of planetesimals. Farther out, it only contains grains which are small enough to develop orbits with sufficiently large apocentric distances due to radiation pressure.

The spatial distribution of material in the same disk is shown in Figure 4. Here, different lines refer to different particle sizes. The ring of the biggest particles shown (100 μm), for which radiation pressure is negligible, nearly coincides with the initial ring of planetesimals (semimajor axes from 27 to 33 AU, eccentricities from 0.0 to 0.2, and hence radial distances from 22 to 40 AU). The larger the particles, the more confined their rings. The rings are more extended outward with respect to the parent planetesimal ring than inward.

Radial profiles of the normal geometrical optical depth for three reference disks (planetesimal rings at 10, 30, and 100 AU) are depicted in Figure 5. Initially, the peak optical depth of the disks is proportional to the distance of the parent ring, making the 100 AU disk 10 times optically thicker than the 10 AU one. The subsequent collisional evolution of the disks depends on their initial mass and distance from the star, as explained in detail in Löhne et al. (2008) and Appendix A. Once a collisional steady state is reached (which is the case after 10 Myr for all three disks), the optical depth decays with time approximately as $t^{-\xi}$, where $\xi \approx 0.3...0.4$, i.e., roughly by 1 order of magnitude from 10 Myr to 10 Gyr. In a steady-state regime, the optical depth is proportional to $r^{1+1.3\xi} \sim r^{1.5}$. This explains why, at any age between 10 Myr and 10 Gyr, the 100 AU ring is ≈30 times optically thicker than the 10 AU one.

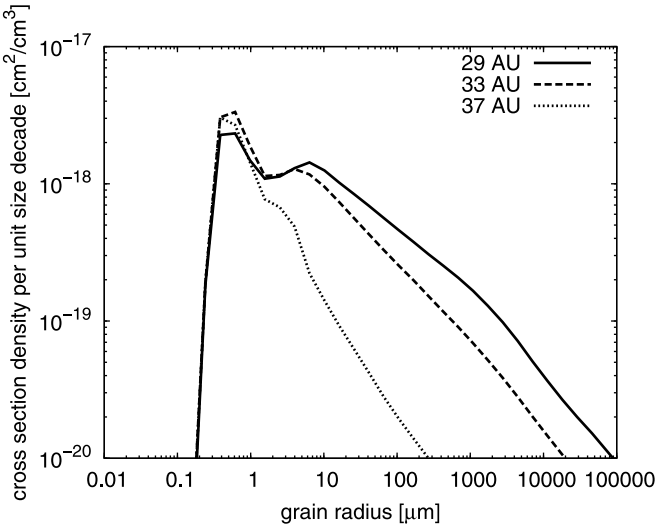

Fig. 3.—Size distribution in the 10EKBD at 30 AU at 100 Myr disk at three different distances from the star.

4.2. *Dust Temperatures*

Figure 6 shows the dust temperatures as a function of two variables: grain distances from the star and their radii. In a parallel scale on the right, we show typical size distributions (cf. Fig. 3). Similarly, under the temperature plot, typical radial profiles of the disk are drawn (cf. Fig. 4). This enables a direct "read-out" of the typical[1] temperature in one or another disk. We find, for example, 130 K at 10 AU, 90 K at 30 AU, and 50 K at 100 AU.

These values are noticeably higher than the blackbody values of 88, 51, and 28 K, respectively. The reason for these big deviations and for the S-shaped isotherms in Figure 6 is the astronomical silicate's spectroscopic properties with relatively high absorption at visible wavelengths and steeply decreasing absorption coefficient at longer wavelengths (see Fig. 2). The cross section–dominating astrosil grains are in a size range where the absorption efficiency for visible and near-infrared wavelengths (around 1 μm) has already reached the blackbody value, while emission is still rather inefficient. With the enhancement of the emission efficiencies relative to the "saturated" absorption, temperatures drop drastically for somewhat larger grains. The larger the distance from the star (yielding lower average temperature

[1] "Typical" in the sense that it is the temperature of cross-section dominating grains in the densest part of the disk.

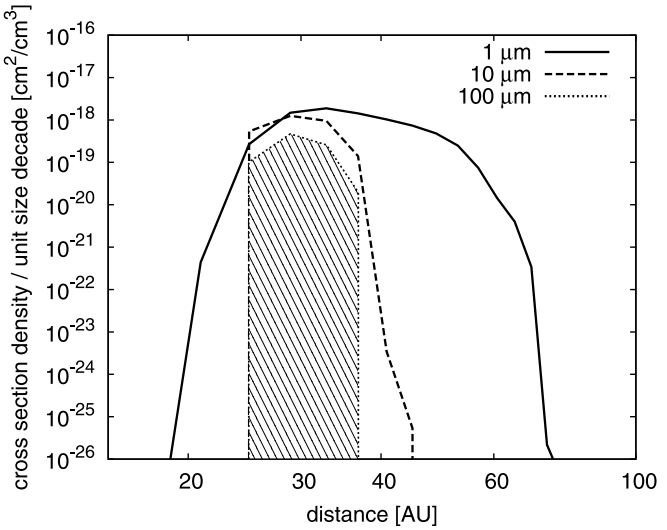

Fig. 4.—Spatial distribution of grains with three characteristic radii for the 10EKBD at 30 AU at 100 Myr disk. The ring of the biggest particles shown (100 μm, *shaded area*) is the narrowest. Its radial extension is nearly the same as that of the initial planetesimal ring; vertical "walls" are artifacts due to a discrete distance binning.

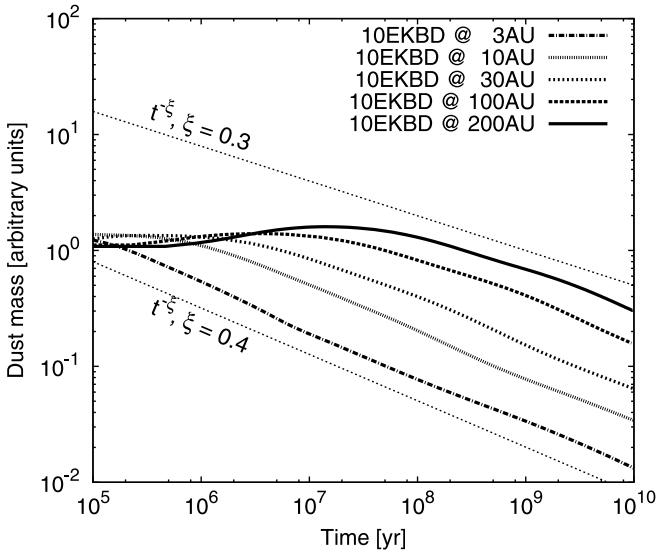

Fig. 12.—Time evolution of dust mass ($s < 1$ mm) for our five reference disks (thick lines). For comparison, power laws with $\xi = 0.3$ and 0.4 are shown with thin dashed lines.

efficiencies and timescales of these processes will be different for different size ranges and different spatial locales in the disk (e.g., Dominik & Farinella 1997; Kenyon & Luu 1998, 1999a, 1999b).

The usefulness of these scaling rules can be illustrated with the following examples.

Example 1.—Assuming now F to be the total amount of dust, from equations (A1)–(A3) one finds

$$F(x M_0; y r; t) \propto x^{1} \; y^{4.3} \, F(M_0; r; t). \qquad (A4)$$

Our choice of reference disks (different distances, but the same volume density) implies $x = y^{-3}$. The normal optical optical depth $\propto F/r^2$ scales as

$$\tau(y^{-3} M_0; y r; t) \propto y^{1-2+3} \, \tau(M_0; r; t). \qquad (A5)$$

Therefore, once a steady state is reached ($\xi = 0.3 \ldots 0.4$), a y times more distant planetesimal belt gives rise to a y^{1-2+3} times optically thicker disk. This explains, in particular, why in Figure 4 any 100 AU ring is 30 times optically thicker than the coeval 10 AU one.

Example 2.—Since the distance r in equations (A1) and (A3) is kept fixed, F in these equations can also denote the radiation flux, emitted by a disk at a certain wavelength. Let $F_o(t)$ be the observed flux from a disk of age t, and imagine a model of a disk of the same age with an initial mass M_0 predicts a flux $F(M_0; t)$ which is by a factor A lower than the observed one:

$$F_o(t) = A \, F(M_0; r; t). \qquad (A6)$$

Our goal is to find the "right" initial mass, i.e., a factor B such that

$$F_o(t) = F(B M_0; r; t). \qquad (A7)$$

With the aid of equation (A1), this can be rewritten as

$$F_o(t) = B F(M_0; r; B t). \qquad (A8)$$

Equation (A3) gives now

$$F_o(t) \propto B F(M_0; r; t) B^{-} = B^{1-} F(M_0; r; t); \qquad (A9)$$

whence

$$B \propto A^{1/(1-)}. \qquad (A10)$$

For instance, a 10 times higher flux at a certain age requires a 427 times larger initial disk mass if $\xi = 0.3 \ldots 0.4$.

Although this rule is convenient for quick estimates, it should be used with caution. As described above, the value of ξ at the beginning of collisional evolution (which lasts up to 100 Myr for the 200 AU belt) can be much smaller—close to zero or even negative—than the "normal" $\xi = 0.3 \ldots 0.4$. For this reason, we prefer to use only the first scaling rule, equation (A1). Therefore, instead of applying equation (A10), we find B by solving equation (A8) numerically with a simple iterative routine. It is this way Figure 11 was constructed.

REFERENCES

Ardila, D. R., et al. 2004, ApJ, 617, L147
Artymowicz, P. 1997, Ann. Rev. Earth Planet. Sci., 25, 175
Aumann, H. H., et al. 1984, ApJ, 278, L23
Beichman, C. A., et al. 2005, ApJ, 622, 1160
———. 2006, ApJ, 639, 1166
Bohren, C. F., & Huffman, D. R. 1983, Absorption and Scattering of Light by Small Particles (New York: Wiley)
Bryden, G., et al. 2006, ApJ, 636, 1098
Burns, J. A., Lamy, P. L., & Soter, S. 1979, Icarus, 40, 1
Carpenter, J. M., Wolf, S., Schreyer, K., Launhardt, R., & Henning, T. 2005, AJ, 129, 1049
Davis, D. R., & Farinella, P. 1997, Icarus, 125, 50
Dohnanyi, J. S. 1969, J. Geophys. Res., 74, 2531
Durda, D. D., & Dermott, S. F. 1997, Icarus, 130, 140
Gladman, B., Kavelaars, J. J., Petit, J., Morbidelli, A., Holman, M. J., & Loredo, T. 2001, AJ, 122, 1051
Grigorieva, A., Artymowicz, P., & Thébault, P. 2007, A&A, 461, 537
Hahn, J. M., & Malhotra, R. 2005, AJ, 130, 2392
Hauschildt, P., Allard, F., & Baron, E. 1999, ApJ, 512, 377
Hayashi, C., Nakazawa, K., & Nakagawa, Y. 1985, in Protostars and Planets II, ed. D. C. Black & M. S. Matthews (Tucson: Univ. Arizona Press), 1100
Hillenbrand, L. A., et al. 2008, ApJ, 677, 630
Kenyon, S. J., & Bromley, B. C. 2005, AJ, 130, 269
Kenyon, S. J., & Luu, J. X. 1998, AJ, 115, 2136
———. 1999a, AJ, 118, 1101
———. 1999b, ApJ, 526, 465
Krivov, A. V., Löhne, T., & Sremčević, M. 2006, A&A, 455, 509
Krivov, A. V., Mann, I., & Krivova, N. A. 2000, A&A, 362, 1127
Krivov, A. V., Sremčević, M., & Spahn, F. 2005, Icarus, 174, 105
Laor, A., & Draine, B. T. 1993, ApJ, 402, 441
Löhne, T., Krivov, A. V., & Rodmann, J. 2008, ApJ, 673, 1123
Metchev, S. A., Hillenbrand, L. A., & Meyer, M. R. 2004, ApJ, 600, 435
Meyer, M. R., et al. 2004, ApJS, 154, 422
Moór, A., Ábrahám, P., Derekas, A., Kiss, C., Kiss, L. L., Apai, D., Grady, C., & Henning, T. 2006, ApJ, 644, 525
Najita, J., & Williams, J. P. 2005, ApJ, 635, 625
Rhee, J. H., Song, I., Zuckerman, B., & McElwain, M. 2007, ApJ, 660, 1556
Rieke, G. H., et al. 2005, ApJ, 620, 1010
Setiawan, J., Weise, P., Henning, T., Launhardt, R., Müller, A., & Rodmann, J. 2007, ApJ, 660, L145
Siegler, N., Muzerolle, J., Young, E. T., Rieke, G. H., Mamajek, E. E., Trilling, D. E., Gorlova, N., & Su, K. Y. L. 2007, ApJ, 654, 580
Spangler, C., Sargent, A. I., Silverstone, M. D., Becklin, E. E., & Zuckerman, B. 2001, ApJ, 555, 932
Stern, S. A., & Colwell, J. E. 1997, ApJ, 490, 879
Stognienko, R., Henning, T., & Ossenkopf, V. 1995, A&A, 296, 797
Su, K. Y. L., et al. 2006, ApJ, 653, 675
Thébault, P., & Augereau, J.-C. 2007, A&A, 472, 169
Thébault, P., Augereau, J.-C., & Beust, H. 2003, A&A, 408, 775
Trilling, D. E., et al. 2007, ApJ, 658, 1289
———. 2008, ApJ, 674, 1086
Williams, J. P., Najita, J., Liu, M. C., Bottinelli, S., Carpenter, J. M., Hillenbrand, L. A., Meyer, M. R., & Soderblom, D. R. 2004, ApJ, 604, 414
Wolf, S., & Hillenbrand, L. A. 2003, ApJ, 596, 603
Wyatt, M. C. 2005, A&A, 433, 1007
Wyatt, M. C., Smith, R., Greaves, J. S., Beichman, C. A., Bryden, G., & Lisse, C. M. 2007, ApJ, 658, 569

COLLISIONAL AND THERMAL EMISSION MODELS OF DEBRIS DISKS: TOWARD PLANETESIMAL POPULATION PROPERTIES

Alexander V. Krivov, Sebastian Müller, Torsten Löhne, and Harald Mutschke
Astrophysikalisches Institut und Universitäts-Sternwarte, Friedrich Schiller University Jena,
Schillergäßchen 2–3, 07745 Jena, Germany; krivov@astro.uni-jena.de
Received 2008 May 21; accepted 2008 July 2

ABSTRACT

Debris disks around main-sequence stars are believed to derive from planetesimal populations that have accreted at early epochs and survived possible planet formation processes. While debris disks must contain solids in a broad range of sizes—from big planetesimals down to tiny dust grains—debris disk observations are only sensitive to the dust end of the size distribution. Collisional models of debris disks are needed to "climb up" the ladder of the colli-